Increasing the stability of perovskite solar cells with Dibenzofulvene-based Hole Transporting Materials

José G. Sánchez,[a] Ece Aktas,[a,1] Eugenia Martínez-Ferrero,[a] Agostina Lina Capodilupo,[b] Giuseppina Anna Corrente,[c] Amerigo Beneduci,[c] Emilio Palomares*[a,d]

[a.] Institute of Chemical Research of Catalonia-The Barcelona Institute of Science and Technology (ICIQ-BIST), Avda. Països Catalans, 16, Tarragona, E-43007, Spain.

E-mail: jgsanchez@iciq.es; eaktas@iciq.es; emartinez@iciq.es; epalomares@iciq.es

[b.] CNR NANOTEC, Institute of Nanotechnology, Campus Ecoteckne, Via Monteroni, 73100 Lecce, Italy.

E-mail: agostina.capodilupo@nanotec.cnr.it

[c.] Department of Chemistry and Chemical Technologies, University of Calabria, Via P. Bucci, Cubo 15D, 87036 Arcavacata di Rende, Italy.

E-mail: amerigo.beneduci@unical.it; giuseppina.corrente@unical.it

[d.] ICREA, Passeig Lluís Companys 23, Barcelona, E08010, Spain.

Abstract

The hole transporting material (HTM) plays a critical role in the performance and stability of perovskite solar cells (PSCs). In PSCs with n-i-p architecture, Spiro-OMeTAD has been widely applied as HTM reaching the highest efficiency, however, its low stability slows down the long-term application of the devices. Thus, in order to enhance the performance of the devices, in this

[1] Present address: Department of Chemical, Materials and Production Engineering, University of Naples Federico II, Piazzale Tecchio 80, 80125 Fuorigrotta, Italy. E-mail: ece.aktas@unina.it

work we analyse, in n-i-p PSCs, three organic hole-transporting materials containing two and three amino redox centers bridged to a dibenzofulvene (**DBF**) backbone. The difference in the molecular structure of the three **DBF**-based HTMs lies in the substitution pattern on the exocyclic fulvene bond. Methodical studies of kinetics and morphology reveal that the nature of the substituent plays a vital role in the performance of the PSC, allowing to obtain an efficiency (16.08 %) comparable to reference Spiro-OMeTAD (17.75 %). In addition, the PSCs with **DBF**-based HTMs demonstrated better stability against the reference prepared with Spiro-OMeTAD under continuous illumination in ambient conditions (15 ± 2 °C and 60 ± 5% RH), as well as under dark and low-humidity conditions. These results place our **DBF**-based organic molecules as promising HTMs to form part of highly efficient and long-term stability perovskite solar cell applications.

Highlights:

- Three dibenzolfulvene derivatives have been tested as hole-transporting materials in PSC

- Champion PCE of 16.08% is obtained with HTM **PN3**.

- The HTM **PN3** contributes to increasing the stability of the cell compared to the reference prepared with Spiro-OMeTAD.

Graphical abstract
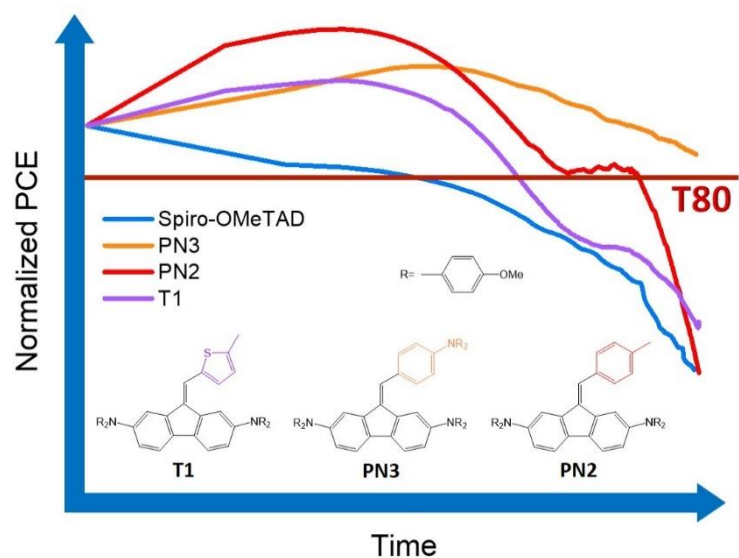
Keywords: perovskite solar cells, dibenzofulvene derivatives, hole transport materials, stability

1. Introduction

The progress in perovskite solar cells (PSCs) has grown rapidly within the last years, yielding devices' efficiency of over 25% [1,2]. Along with the high efficiencies, the low-cost fabrication methods and outstanding optoelectronic properties of the perovskite photoactive layer, such as high optical absorption, tuneable bandgap energy, long charge-carrier diffusion length, high charge-carrier mobility and low exciton binding energy, make of the PSCs a competitive alternative to form part of the photovoltaic market [3–6]. To achieve the current high efficiency in PSCs, several strategies have been followed such as improving the quality of the perovskite film, developing the device configuration structure, or the engineering of the cathode and anode. For the first strategy, uniform perovskite film with high crystallinity, large grain size, and grain orientation have been achieved using solvent engineering approaches, e.g., mixing solvents, antisolvent, vapour assisted process, etc. [7–9]. Regarding the device configuration, the structure of PSCs includes a perovskite absorber placed between an electron transport material (ETM) and a hole transport material (HTM). The structural configuration of PSCs can be classified into two types: regular (n-i-p) and inverted (p-i-n) structures, depending on the position of the charge transport materials in face of the substrate. Besides, the regular structure can be divided into mesoscopic and planar configurations depending on the structure of the ETM. In all the cases, (either regular or inverted) it is critical to choose suitable HTM and ETM since the performance of the devices is intimately related to their characteristics.

On one hand, in inverted PSCs (iPSCs) the most common ETMs used are the bilayers consisting of [6,6]-phenyl-C61-butyric acid methyl ester (PCBM) and bathocuproine (BCP) or C60/BCP. Similarly, the polymers poly(3,4-ethylenedioxythiophene):poly(styrenesulfonate) (PEDOT:PSS) and the poly[bis(4-phenyl) (2,4,6-trimethylphenyl) amine] (PTAA) are the most common HTMs [10,11]. However, several new organic small molecules and self-assembled monolayers have been

4

designed as HTMs giving highly efficient and stable iPSCs [12–16]. On the other hand, in mesoscopic and planar regular PSCs, the titanium oxide (TiO_2) and tin oxide (SnO_2) are the most used ETM, respectively. In addition to TiO_2 and SnO_2, some inorganic materials such as zinc oxide (ZnO), cadmium sulfide (CdS), aluminium oxide (Al_2O_3) have been tested as well [1,17–21]. Regarding the HTM, the 2,20,7,70-tetrakis-(N,N-di-4-methoxyphenylamino)-9,90-spirobifluorene (Spiro-OMeTAD) is the HTM of choice in regular n-i-p PSCs (either mesoscopic or planar configuration) and it holds the record for the highest efficiency of n-i-p PSCs [1,2,19]. However, this molecule presents some drawbacks like its high cost, due to complex synthetic route and highly-cost purification; significant low hole-mobility in neat form that requires chemical doping to increase the hole-mobility; and low moisture-and temperature-resistance which limits the long-term stability of devices [22–24]. Thus, several efforts have been made to design HTMs able to efficiently extract the holes from the perovskite, and simultaneously increase the device's long-term stability. The structure of the HTMs can be classified according to their core structure. The first are based on the spiro-linked structure, in which two molecular π-systems are connected to a common sp^3-hybridized atom [25–28]. The second type of HTMs refers to all those without spiro-linked structures, which can be divided into two subcategories: one-dimension linear small molecules, and two- and three-dimension star-shaped small molecules [28–33]. For example, the dibenzofulvene (DBF) core allows the design of star shaped molecules where electron rich phenyl amines substituents are bonded to a central π core. The DBF unit is easily synthesized and constitutes a versatile building block since it can be functionalized at different positions of the benzene.[34–36] Encouraged by these characteristics, several authors have designed novel HTMs containing a DBF-core with phenylamine lateral substituents, but varying the substituent linked to the exocyclic fulvene bond [37–39]. Y-C Chen et. al have recently reported the comparison of a triphenylamine dibenzofulvene–based HTMs substituted with zero, four and six methoxy groups in the preparation of efficient inverted PSCs [40]. The dopant-free molecule promoted the growth of

the perovskite layer with lower concentration of defects, and therefore, higher performance and stability.

In the present study, we report the preparation of PSC using three one-dimensional planar HTMs containing two phenylamine substituents connected to a dibenzofulvene (**DBF**) core, where a different substituent is linked to the exocyclic fulvene bond (see Figure 1a). **PN3** is an asymmetric triphenylamine dibenzofulvene compound with six external methoxy groups. **PN2** and **T1** are biphenylamine dibenzofulvene compounds with four methoxy groups and a phenyl or a thiophene substituent bonded to the exocyclic fulvene, respectively (Figure 1a). We have investigated the effects of the substituent in the exocyclic fulvene on the performance parameters and stability of PSCs. To do so, PSCs with regular n-i-p mesoporous structure based on the caesium-containing triple cation (CsFAMA) perovskite were fabricated using the **DBF**-based molecules as HTM. Devices with the popular Spiro-OMeTAD molecule as HTM were prepared as reference because of its high efficiency. The three **DBF**-based HTMs successfully demonstrate the reduction of the trap-assisted recombination degree in comparison to the reference device. Among the **DBF**-based HTMs, the device with **PN3** shows the highest PCE (16.08 %), which is comparable to the 17.75% obtained with the reference Spiro-OMeTAD. More interestingly, our result reveals that PSCs fabricated with the **DBF**-based HTMs are more stable, where those with **PN3** exhibited the longest lifetime.

2. Experimental methods

2.1 Characterization of the molecules

The synthesis-route, and the nuclear magnetic resonance, mass spectrometry and optical and electrochemical characterization of the **DBF**-based HTMs have been described as reported in references [41,42].

Thermogravimetric analysis (TGA) was done in a Mettler Toledo TGA/SDTA851 thermogravimetric balance under a nitrogen atmosphere following a ramp from 50 to 900 °C at a heating rate of 10 °C/min. Differential Scanning Calorimetry (DSC). DSC measurements were done in a Mettler Toledo 822e differential scanning calorimeter under a nitrogen atmosphere following a ramp from 30 to 300 °C at a heating rate of 10 °C/min.

2.2 Device fabrication

The solar cell devices were fabricated onto patterned fluorine-tin oxide (FTO) glass substrates. FTOs substrates were sequentially cleaned with an alkaline cleaning concentrate (Hellmanex) diluted in deionized water, acetone, methanol and isopropanol in an ultrasonic bath for 15 min. Then, they were dried with dry nitrogen flow and treated in a UV-ozone cleaner for 30 min. Compact titania (c-TiO$_2$) layer was deposited onto the FTOs substrates by spray pyrolysis technique. A solution of titanium diisopropoxide bis(acetylacetonate) dissolved in acetylacetonate and ethanol was sprayed on FTOs at 450 °C. Subsequently, a mesoporous TiO$_2$ (mp-TiO$_2$) layer was obtained by spin-coating a titania solution with a 30 nm particle size at 4000 rpm for 30 s followed by an annealing step at 450 °C by 30 min. The mp-TiO$_2$ solution was prepared by dissolving a commercial titania paste (30NR-D, Greatcell) in ethanol (ratio 1:7 by weight). Then, bis(trifluoromethane)sulfonimide lithium salt (Li-TFSI) was dissolved in acetonitrile (10 mg mL^{-1}) and spin-coated at 3000 rpm onto the mp-TiO$_2$ layer. The substrates were then immediately annealed at 40 °C for 30 min. To obtain the CsFAMA perovskite layer, the perovskite precursor solution [(FAPbI$_3$)$_{0.83}$(MAPbBr$_3$)$_{0.17}$]$_{0.95}$[CsPbI$_3$]$_{0.05}$ was spun on top of the titania layer by 4000 rpm for 40 s. 15 s prior to the end of the spin-coating sequence, 250 µl of Anisole was dropped onto the spinning substrate. Then, the samples were annealed at 100 °C for 1h. The perovskite precursor solution was prepared by dissolving PbBr$_2$ (1.5M) and PbI$_2$ (1.5M) in a mixed solution of N,N-dimethylformamide and dimethyl sulfoxide (DMF:DMSO with a ratio of 4:1 by volume). The

$PbBr_2$ and PbI_2 solutions were added to methylammonium bromide (MABr) and formamidinium iodide (FAI) powders, respectively, to obtain $MAPbBr_3$ and $FAPbI_3$ solutions with a final concentration of 1.24 M. Then, $MAPbBr_3$ and $FAPbI_3$ solutions were mixed in a 17:83 volume ratio. Finally, the cesium iodide (CsI) dissolved in DMSO (1.5 M) was added with a ratio of 95:5 by volume. The **DBF**-based and Spiro-OMeTAD hole-transporting materials were dissolved in chlorobenzene in advance and spin-coated onto the perovskite layer. The optimized concentration of HTMs was 15 mM for **T1**, **PN2** and **PN3**, and 25 mM for Spiro-OMeTAD. All the HTMs were doped with Li-TFSI, 4-tert-butylpyridine (tBP), and tris(2-(1H-pyrazol-1-yl)-4-tert-butylpyridine)cobalt(III) tri[bis(trifluoromethane)sulfonimide] (Co-TFSI). Finally, samples were transferred to the glove box where 80 nm of gold (top electrode) was thermally evaporated under high vacuum conditions through a shadow mask to define the area of the device (0.09 cm^2). The hole-only devices were fabricated with the structure ITO/PEDOT:PSS/HTM/Au. PEDOT:PSS was spin-coated onto the ITO at 4000 rpm for 40 s and then annealed at 150 °C for 10 min under ambient conditions. Then, the HTMs were spin-coated on top of PEDOT:PSS under the same conditions as PSC devices. The film thickness of HTMs is ~100 nm. Finally, 80 nm of gold were thermally evaporated under high vacuum conditions.

2.3 Device characterization

The illuminated current density–voltage (*J-V*) characteristics were recorded by a Keithley 2400 source-measurement unit in forward (from -0.2V to 1.2V) and reverse (from 1.2V to -0.2V) scan at room temperature and nitrogen atmosphere. The illumination measurements were carried out using the solar simulator Abet Technologies model 11000 class type A; Xenon arc; AM 1.5 G irradiation (100 mW/cm^2). The light intensity was modulated by optical filters. The EQE measurements were performed under short-circuit conditions with the wavelength sweep from 300 nm to 800 nm using a xenon arc lamp coupled to a Cornerstone 130B monochromator as light

source, and a Newport 2936-R power-meter unit (Lasing, S.A.; IPCE-DC, LS1109-232). Steady-state photoluminescence (PL) and transient photoluminescence (TRPL) measurements were conducted on a fluorescence lifetime spectrometer (LifeSpec II, Edinburgh Instruments) integrated with a photomultiplier tube (PMT) detector, double subtractive monochromator and 635 nm picosecond laser. Atomic force microscopy measurements (AFM) were performed in tapping mode on a Molecular Imaging model Pico SPM II (pico+). Images were recorded in air conditions using silicon probes with a radius of 2-3 nm and at the resonant frequency of 150 kHz. The surface morphology images of neat CsFAMA and CsFAMA/HTMs films were recorded by a field emission scanning electron microscope (FESEM, FEI Quanta 600 microscopy).

3. Results and Discussion

3.1 Thermal and electrical characterization of the molecules

The thermal stability and decomposition studies of the molecules was performed by thermogravimetric analysis (TGA) and differential scanning calorimetry (DSC) (Figure S1, ESI†). The results from TGA and DSC characterization are listed in Tables S1 and S2, ESI. The reference Spiro-OMeTAD shows a first decomposition step at 163 °C followed by the main inflection point at 456 °C, in agreement to values reported in the literature [43]. **T1** decomposes at a single step at 455 °C. **PN2** and **PN3** show a first decomposition step at temperatures below 200 °C, although only **PN2** has a higher than 5% weight loss, and a second more pronounced step at 454 and 439 °C, respectively. Interestingly, **PN2** and **PN3** have a third thermal decomposition step at higher temperatures around 580 °C. All the HTM molecules show excellent thermal stability that makes them suitable for solar cells applications. Regarding DSC measurements, the Spiro-OMeTAD show a glass transition temperature at 163 °C and melting point at 248 °C, in agreement with the literature [40]. The **T1** molecule show a glass transition temperature at 142 °C, **PN2** show two

endothermic processes at 98 and 153 °C whereas **PN3** has an endothermic transition at 83 °C and an exothermic process at 172 °C.

The hole-mobility of **DBF**-based molecules were assessed by the space charge limited current (SCLC) method [44] using hole-only devices with the structure ITO/PEDOT:PSS/HTM/Au, and were determined to be 7.4×10^{-4} cm^2 V^{-1} s^{-1} for Spiro-OMeTAD, 9.2×10^{-5} cm^2 V^{-1} s^{-1} for **PN3**, 4.5×10^{-5} cm^2 V^{-1} s^{-1} for **PN2**, and 1.1×10^{-4} cm^2 V^{-1} s^{-1} for **T1** (Figure S2). Among the **DBF**-based molecules, **PN3** and **T1** have similar hole-mobility, whereas **PN2** displays the lowest values; however, all of them show lower hole mobility compared to that of the reference Spiro-OMeTAD (Table S3).

3.2 Photovoltaic properties

To evaluate the photovoltaic performance of the **DBF**-based molecules as HTM, we fabricated caesium-containing triple cation (CsFAMA) perovskite solar cells. PSCs with Spiro-OMeTAD as HTM were fabricated as reference. As shown in Figure 1b, the PSCs were fabricated in a regular mesoporous configuration with the structure FTO/compact TiO$_2$/LiTFSI-doped mesoporous TiO$_2$/CsFAMA/HTM/Au. Figure 1c displays the energy levels alignment of HTMs and perovskite, using values taken from the literature [15,25,41,42,45]. On the one hand, **PN3** and **PN2** showed similar deep HOMO energy levels (-5.14 and -5.12 eV, respectively) which matches well with the valence band of CsFAMA, while the one of **T1** showed the lowest HOMO energy level (-4.75 eV). On the other hand, the LUMO energy level of the three molecules (**PN3** = -2.67eV, **PN2**= -3.01eV, and **T1**= -2.77eV) is higher than the conduction band of CsFAMA, although, the **PN3** has the highest LUMO which ensures a better electron blocking from the perovskite.

The performance parameters of the PSCs were extracted from the current-density vs. voltage characteristics (*J-V*) measured under standard illumination conditions (100 mW/cm^2). Figure 2a shows the *J-V* characteristics for the best-performing PSCs, and the corresponding photovoltaic

parameters are summarized in Table 1. The champion device with **PN3** shows a PCE of 16.08 %, with a J_{SC} = 20.83 mA/cm^2, V_{OC} = 1.046 V, and FF = 73.82 %, which is slightly lower than that of the reference one, which exhibited the highest PCE (17.75%), with a J_{SC} = 21.86 mA/cm^2, V_{OC} = 1.086 V, and FF = 74.73 %. In the case of the champion device with **PN2**, the lower PCE (15.29 %) is mainly due to its lower V_{OC} (0.952 V) since it showed a similar J_{SC} and FF (21.59 mA/cm^2, 74.38 %, respectively) than that of the reference device. The champion device with **T1** exhibited the lowest PCE (13.53 %) among all the molecules due to its low V_{OC} (0.918 V), which could be related to the higher mismatch between the HOMO energy level of the **T1** and the valence band maximum of CsFAMA. [42]

To validate the performance parameters extracted from *J-V* curves, we carried out external quantum efficiency measurements for all the PSCs. Figure 2b displays the EQE spectra and the integrated J_{SC} for PSCs with different **DBF**-based HTMs and the reference incorporating Spiro-OMeTAD as HTM. Compared to the reference, the EQE of the device employing **PN2** HTM is significantly higher in the range of 350-550 nm, whereas PSCs with **PN3** and **T1** exhibited similar EQE values to that of the reference PSC in this region. The EQE values of devices with the three different **DBF**-based HTMs slightly decreases in the range 550-750 nm. The integrated J_{SC} values calculated from EQE spectra are displayed in Table 1. The $J_{SC\text{-}EQE}$ values correspond to those extracted from *J-V* curves.

3.3 Light intensity dependence of *J-V* characteristics

The *J-V* characteristics measurements as a function of light intensity (P_{light}) were used to study the effects of **DBF**-based HTMs on the recombination mechanisms in photovoltaic devices. Figure 3a shows the J_{SC} against P_{light} plot of all devices fitted by the power-law function $J_{SC} \propto P_{light}{}^{\alpha}$, where α indicates the bimolecular recombination degree. The PSCs with Spiro-OMeTAD, **PN3**, **PN2** and **T1** showed a linear correlation with similar α values (0.94, 0.94, 0.96, and 0.95, respectively). The

α values close to 1 indicate that bimolecular recombination is not significant under short circuit conditions, therefore, we have considered that this type of recombination is not determining the behaviour of the devices. On the other hand, the trap-assisted recombination degree was estimated by fitting the light intensity-dependent V$_{OC}$ curves of all PSCs by the equation $V_{OC} \propto (n_{id}kT/q) \, ln(P_{light})$, where the ideality factor (n_{id}) indicates the trap-assisted recombination degree, k is the Boltzmann constant, T is the temperature, and q is the particle charge. As shown in Figure 3b, the n_{id} values of PSCs with Spiro-OMeTAD, **PN3**, **PN2**, and **T1** were calculated to be 1.71, 1.26, 1.06, and 1.06, respectively. The low n_{id} values indicate that trap-assisted recombination is suppressed in devices using **DBF**-based HTMs more efficiently in comparison to that using Spiro-OMeTAD. These results suggest that there is reduced surface defect and higher charge extraction capacity at the perovskite/HTM interface of devices prepared with **PN3**, **PN2** and **T1**.

3.4 Photoluminescence measurements

To gain insight into the charge carrier dynamics at the interface CsFAMA/HTMs and hole extraction ability, we carried out steady-state photoluminescence (PL) and time-resolved photoluminescence (TRPL) measurements. The PL spectra of neat CsFAMA and CsFAMA/HTMs films are depicted in Figure 4a. The stacked CsFAMA/HTMs systems exhibited a much lower PL intensity regarding neat CsFAMA film, which indicates all the HTMs quench the perovskite emission signal in similar order. As shown in the inset of Figure 4a, the PL-intensity peaks decreased by about 95.6%, 95.9%, 96.9%, and 97.4% from the perovskite PL-emission by using the **PN3**, Spiro-OMeTAD, **PN2** and **T1** as HTM, respectively. The higher PL-quenching by **PN2** and **T1** compared to that of Spiro-OMeTAD is attributed to a more efficient hole extraction ability of these **DBF**-based HTMs than Spiro-OMeTAD. Figure 4b displays the fluorescence decay in the

CsFAMA/HTMs samples. The fitting of decays was done using the following bi-exponential

equation (see Equation 1):

$$\tau(t) = A_1 e^{-\left(\frac{t}{\tau_1}\right)} + A_2 e^{-\left(\frac{t}{\tau_2}\right)} \quad \text{(Equation1)}$$

where A1 and A2 are the amplitude of the radiative decay lifetime and τ represent the lifetime

values. The average decay lifetimes match with the observations made from the PL spectra. On

the other hand, all the samples shown a fast (τ_1) and slow (τ_2) decay lifetimes. The slow decay

time τ_2 is attributed to radiative recombination of charge carrier due to defects in the bulk.

However, the fast decay lifetime τ_1 is attributed to non-radiative recombination (e.g., trap-

assisted recombination) due to surface defects in the neat CsFAMA film, whereas in CsFAMA/HTM

films the τ_1 is the result of the charge carriers quenching at the perovskite/HTM interface [46,47].

The fitting parameters are summarized in Table S4, ESI†. As expected, the neat CsFAMA showed

the longest lifetime. Compared to CsFAMA/Spiro-OMeTAD, the shorter τ_1 of CsFAMA/**PN2** and **T1**

revealed a faster hole extraction from CsFAMA layer by the **PN2** and **T1** with lower recombination

losses. The CsFAMA/**PN3** exhibited slightly lower τ_1 than that of CsFAMA/Spiro-OMeTAD,

suggesting fewer recombination. Since the A1 and A2 are the weighting parameters, we can

assume which component dominates the PL decay in the different samples. The samples with **PN2**

and **T1** have higher A1 values than that of A2, indicating the PL decay is governed by the charge

carrier quenching due to a good hole extraction process. Meanwhile, the higher value of A2 of

samples with Spiro-OMeTAD and **PN3** suggests the PL decays due to higher recombination losses

before the holes are extracted. The results from PL and TRPL analysis suggest that **T1** and **PN2**

reduce the charge recombination at the interface CsFAMA/HTM, which can be correlated to the

lower trap-assisted recombination observed in the data of Figure 3b. In the case of **PN3**, the PL

peak intensity is slightly higher than that of Spiro-OMeTAD, thus, it can be inferred that both HTMs have similar hole extraction capability and charge recombination at the perovskite/HTM interface. However, devices with Spiro-OMeTAD exhibited a higher trap-assisted recombination degree than that of devices with **PN3** (Figure 3b).

3.5 Morphological characterization of the films

Morphological studies of the films deposited on top of the perovskite have been carried out by AFM and FESEM. Figure 5 shows the height and phase (AFM) and FESEM images of the HTM molecules deposited on top of the perovskite and the perovskite as a reference. In the AFM images, the CsFAMA perovskite forms granulated films with clear domains that result in a rough surface. The Spiro-OMeTAD forms homogeneous films on top of the perovskite ensuring a full coverage that also decreases the roughness one order of magnitude. The **DBF** derivatives do also decrease the roughness of the perovskite film. The three molecules form films with decreasing roughness from 4.7 of **T1** to 4.05 nm for **PN3** that are formed by small crystallites that can even form mountains and valleys in the case of **T1**. **PN3** is more homogeneous due to the three similar peripheric substituents that enhance the interaction between them. FESEM images confirm these observations. In the case of Spiro-OMeTAD, the morphology of the film is difficult to appreciate due to its smoothness whereas the **DBF** derivatives form structured domains that cover all the surface of the perovskite. No pinholes can be appreciated by this technique.

Taking into account the PL measurements, the methoxy group present in Spiro-OMeTAD and **PN3** facilitates the formation of smoother surfaces on top of the perovskite. On the contrary, they extract holes and passivate with less efficiency the surface of the perovskite, so the trap-assisted recombination is higher than **PN2** and **T1**.

3.6 Devices stability test

As shown in Figure 2a, all the devices using **DBF**-based HTMs have higher J-V hysteresis in comparison with the reference. However, the device with **PN3** exhibited the lowest J-V hysteresis among the devices using **DBF**-based HTMs, whereas the device with **T1** showed the highest one. However, the hysteretic behaviour on all the PSCs decreased when devices are exposed to a dry-air atmosphere (constant synthetic airflow of ~10 % RH under dark conditions) over time. We calculated the hysteresis index (HI), HI = ($PCE_{reverse}$ − $PCE_{forward}$)/$PCE_{reverse}$) [38], to evaluate the variations of the degree of hysteresis after air exposition. The HI of devices with Spiro-OMeTAD decreased from 0.37 to 0.13, while the HI of devices with **DBF**-based HTMs decreased from 0.41, 0.58 and 0.66 to 0.27, 0.26 and 0.16 for **PN3**, **PN2**, and **T1**, respectively. The devices with **PN2** and **T1** showed a higher hysteresis decrease than those with Spiro-OMeTAD and **PN3**, which may suggest a better enhancement of their hole-mobility and hole-extraction properties with time, and the decrease of charge traps at the perovskite/HTM interface. Figure S3, ESI† shows J-V characteristics, and Table S5, ESI† summarizes detailed performance parameters of devices after 12 days of exposition to air. To determine the stability of PSCs, we monitored the PCE of devices with Spiro-OMeTAD with that of devices with **DBF**-HTMs over time (Figure 6a). On one hand, the stability test was carried out under continuous one sun illumination in ambient conditions (15 ± 2 °C and 60 ± 5% RH). As shown in Figure 6a, the PSCs with **DBF**-based HTMs have higher stability than the devices with Spiro-OMeTAD. Commonly, the time in which the PCE drops 20% from the initial value (so-called t_{80}) is used as a figure of merit for the stability. The Spiro-OMeTAD device displays a rapid decay in the first 10 min and decreases 15% of its initial PCE, then, it reaches 80% of its PCE remaining after 50 min (t_{80}). Opposite to Spiro-OMeTAD, the PSCs with the **DBF**-based HTMs have increased up until reached their maximum PCEs (20 min for **PN2** and **T1**, and 50 min for **PN3**), then experienced an exponential decay. The devices with **PN2** and **T1** showed similar stability behaviour to each other, however, the t_{80} of **PN2** is higher than that of **T1** (300 min and

200 min, respectively). Unlike the PSCs with **PN2** and **T1**, the ones with **PN3** did not reach the t_{80} during the measurement time, thus it can be inferred that its t_{80} could be higher than 1000 min. On the other hand, stability was tested in long-term ageing studies under low-humidity ambient conditions (10% RH). To do so, all the samples were stored under dark conditions with a constant synthetic airflow of ~10 % RH over 95 days. Figure 6b shows the *J-V* characteristics of the best-performing fresh (as prepared) and degraded (stored in dark for 95 days) devices with the different HTMs under reverse scan. The comparison of the performance parameters of fresh and degraded devices is presented in Table S6, ESI†. In all devices, the J_{SC} and FF decreased after 95 storing days, whereas the V_{OC} slightly increased. Moreover, the hysteresis has been reduced in samples with Spiro-OMeTAD (HI = 0.04), **PN3** (HI = 0.04), and **PN2** (HI = 0.09), whereas samples with **T1** still present high hysteresis (HI = 0.25) after 95 days (see Figure S5, ESI†). From Figure 6b, it was also noticed a decrease in the slope at V_{OC} of degraded devices, which is attributed to the increment of the series resistance (R_S). It is well known that the increment of R_S has an opposite effect on the FF, decreasing the PCE of the device. The R_S of all fresh and degraded devices were extracted from *J-V* curves and summarized in Table S6, ESI†. The R_S of all devices increases after 95 days of storing: Spiro-OMeTAD from 4.35 to 10.21 $\Omega \cdot cm^2$, **PN3** from 5.18 to 6.58 $\Omega \cdot cm^2$, **PN2** from 4.41 to 8.62 $\Omega \cdot cm^2$, and **T1** from 5.58 to 9.43 $\Omega \cdot cm^2$. The R_S of degraded PSC with Spiro-OMeTAD increases more than double that of fresh one (2.34 times higher), whereas R_S of **DBF**-based degraded devices were 1.27, 1.96 and 1.67 times higher for **PN3**, **PN2** and **T1**, respectively. In addition, comparing the PCE of all fresh and degraded devices (see Table S6, ESI†), we observed that their efficiency decreased more than 10% from its initial PCE (as prepared). The PCE of devices decreased in the sequence **PN3** (10%), **PN2** (11%), **T1** (14%), and Spiro-OMeTAD (19%). This trend agrees with that observed in Figure 6a, which confirms the **DBF**-based HTMs successfully enhanced the stability of CsFAMA-based PSCs regarding the Spiro-OMeTAD. The lifetime of devices with **PN3** is twice longer than that of the control device. The limited stability of

16

PSCs with doped Spiro-OMeTAD is attributed to the rapid degradation of the HTM film caused by the hygroscopicity nature of the LiTFSI [48]. On the other hand, the higher stability of devices with **PN3** indicates the Li-TFSI dopant has no effects on the **PN3** film. A recent study has demonstrated the high hydrophobic character of triphenylamine dibenzofulvene-based molecules can successfully suppress the effects of the Li-TFSI dopant [39]. The higher stability of the devices with **PN3** is therefore assigned to the compact film formed by the **PN3** film in comparison to **PN2** and **T1** (see Figure 5), which reduces the pathways for the moisture infiltration that degrades the perovskite film.

Finally, we performed the P_{light}-dependence of V_{OC} and J_{SC} measurements on all devices stored in dark to analyze the effects of degradation on the recombination kinetics. On one hand, the analysis of the J_{SC} vs. P_{light} plot (Figure S6a, ESI†) reveals that there is not any significant change in the bimolecular recombination under short circuit conditions for all devices after 95 storing days. On the other hand, the results from the V_{OC} vs. P_{light} (Figure S6b, ESI†) showed that the trap-assisted recombination degrees increased in all the devices over storing time, however, the devices with Spiro-OMeTAD and **PN3** exhibited a higher trap-assisted recombination degree compared to those with **PN2** and **T1** (2, 1.70, 1.32, and 1.15, respectively). These results confirm that, even though, **PN3** has the highest trap-assisted recombination degree among the **DBF**-based HTMs, still the three **DBF**-based HTMs show lower recombination degree than Spiro-OMeTAD, suggesting that indeed the common aromatic group connected to the **DBF** core plays an important role to suppress the trap assisted recombination at the CsFAMA/HTM interlayer for fresh (Figure 3b) and degraded (Figure S6b) devices.

4. Conclusion

In summary, three organic hole-transporting materials, **PN3**, **PN2** and **T1**, with two and three amino redox centers bridged to a dibenzofulvene backbone have been tested as HTM in n-i-p PSCs. All HTMs consist of a **DBF** core with a different substituent linked in the exocyclic fulvene bond, where **T1** incorporates a thiophene substituent, **PN2** a phenyl, and **PN3** a third phenylamine substituted with methoxy groups. **PN3** and **PN2** HTMs showed similar HOMO energy levels to Spiro-OMeTAD, whereas **T1** had a lower HOMO energy level which contributed to a lower V_{OC} in the PSC. The thiophene substituent provides higher hole mobility to **T1**, on the contrary, the phenyl substituent limits the hole mobility in **PN2**. However, all the **DBF**-based HTMs exhibited lower hole mobility regarding Spiro-OMeTAD as calculated from the SCLC measurements. Among the PSCs with **DBF**-HTM, the champion PSCs were fabricated using **PN3** HTM with a PCE of 16.08% comparable to those of Spiro-OMeTAD reference with a PCE of 17.75%. In comparison to Spiro-OMeTAD reference, the trap-assisted recombination is highly reduced by **DBF**-based HTMs in the perovskite/HTM interface. Despite the **T1** and **PN2** show faster hole extraction than Spiro-OMeTAD, PSCs with these HTMs exhibited lower efficiencies. The good performance of the device with **PN3** HTM is ascribed to the well-match energy level alignment between **PN3** and perovskite and a uniform HTM film, as well as effective charge extraction and suitable hole mobility. In contrast, the poor efficiency of devices with **T1** could be attributed to the energy losses due to the highest bandgap difference between the valance band of CsFAMA and HOMO level of **T1**. Whereas the efficiency of devices with **PN2** could be limited by the low hole mobility of **PN2**. More importantly, the PSCs with **DBF**-based HTMs demonstrated better long-term stability to the Spiro-OMeTAD reference. Despite the devices with **PN3** show slightly lower performance parameters than the popular Spiro-OMeTAD, its stability is at least twice longer probably due to its protective effect on the perovskite film that prevents degradation from ambient conditions. These results place **PN3** as a promising organic HTM for highly efficient and long-term stable PSCs.

Declaration of Competing Interest

The authors declare no competing financial interest.

Acknowledgments

References

[1] H. Min, D.Y. Lee, J. Kim, G. Kim, K.S. Lee, J. Kim, M.J. Paik, Y.K. Kim, K.S. Kim, M.G. Kim, T.J. Shin, S. il Seok, Perovskite solar cells with atomically coherent interlayers on SnO2 electrodes, Nature. 598 (2021) 444–450. https://doi.org/10.1038/s41586-021-03964-8.

[2] J. Jeong, M. Kim, J. Seo, H. Lu, P. Ahlawat, A. Mishra, Y. Yang, M.A. Hope, F.T. Eickemeyer, M. Kim, Y.J. Yoon, I.W. Choi, B.P. Darwich, S.J. Choi, Y. Jo, J.H. Lee, B. Walker, S.M. Zakeeruddin, L. Emsley, U. Rothlisberger, A. Hagfeldt, D.S. Kim, M. Grätzel, J.Y. Kim, Pseudo-halide anion engineering for α-FAPbI3 perovskite solar cells, Nature. 592 (2021) 381–385. https://doi.org/10.1038/s41586-021-03406-5.

[3] P. Wang, Y. Wu, B. Cai, Q. Ma, X. Zheng, W.-H. Zhang, Solution-Processable Perovskite Solar Cells toward Commercialization: Progress and Challenges, Advanced Functional Materials. 29 (2019) 1807661. https://doi.org/https://doi.org/10.1002/adfm.201807661.

[4] S. Park, J.H. Heo, C.H. Cheon, H. Kim, S.H. Im, H.J. Son, A [2,2]paracyclophane triarylamine-based hole-transporting material for high performance perovskite solar cells, Journal of Materials Chemistry A. 3 (2015) 24215–24220. https://doi.org/10.1039/C5TA08417B.

[5]   S. Meloni, T. Moehl, W. Tress, M. Franckevičius, M. Saliba, Y.H. Lee, P. Gao, M.K. Nazeeruddin, S.M. Zakeeruddin, U. Rothlisberger, M. Graetzel, Ionic polarization-induced current–voltage hysteresis in CH3NH3PbX3 perovskite solar cells, Nature Communications. 7 (2016) 10334. https://doi.org/10.1038/ncomms10334.

[6]   J. Lim, M.T. Hörantner, N. Sakai, J.M. Ball, S. Mahesh, N.K. Noel, Y.-H. Lin, J.B. Patel, D.P. McMeekin, M.B. Johnston, B. Wenger, H.J. Snaith, Elucidating the long-range charge carrier mobility in metal halide perovskite thin films, Energy & Environmental Science. 12 (2019) 169–176. https://doi.org/10.1039/C8EE03395A.

[7]   Z. Tang, S. Tanaka, S. Ito, S. Ikeda, K. Taguchi, T. Minemoto, Investigating relation of photovoltaic factors with properties of perovskite films based on various solvents, Nano Energy. 21 (2016) 51–61. https://doi.org/https://doi.org/10.1016/j.nanoen.2015.12.013.

[8]   S. Ghosh, S. Mishra, T. Singh, Antisolvents in Perovskite Solar Cells: Importance, Issues, and Alternatives, Advanced Materials Interfaces. 7 (2020) 2000950. https://doi.org/https://doi.org/10.1002/admi.202000950.

[9]   M. Liu, M.B. Johnston, H.J. Snaith, Efficient planar heterojunction perovskite solar cells by vapour deposition, Nature. 501 (2013) 395–398. https://doi.org/10.1038/nature12509.

[10]   N. Wanyi, T. Hsinhan, A. Reza, B. Jean-Christophe, N.A. J, G. Gautam, C.J. J, C. Manish, T. Sergei, A.M. A, W. Hsing-Lin, M.A. D, High-efficiency solution-processed perovskite solar cells with millimeter-scale grains, Science (1979). 347 (2015) 522–525. https://doi.org/10.1126/science.aaa0472.

[11]   D. Matteo, A. Qingzhi, A.-S. Miguel, H.Y. J, C. Changsoon, P. Fabian, G. Giulia, V. Yana, 23.7% Efficient inverted perovskite solar cells by dual interfacial modification, Science Advances. 7 (2022) eabj7930. https://doi.org/10.1126/sciadv.abj7930.

[12]   X. Lai, M. Du, F. Meng, G. Li, W. Li, A.K.K. Kyaw, Y. Wen, C. Liu, H. Ma, R. Zhang, D. Fan, X. Guo, Y. Wang, H. Ji, K. Wang, X.W. Sun, J. Wang, W. Huang, High-Performance Inverted

Planar Perovskite Solar Cells Enhanced by Thickness Tuning of New Dopant-Free Hole

Transporting Layer, Small. 15 (2019) 1904715.

https://doi.org/https://doi.org/10.1002/smll.201904715.

[13]   W. Yu, J. Zhang, X. Wang, X. Liu, D. Tu, J. Zhang, X. Guo, C. Li, A Dispiro-Type Fluorene-

Indenofluorene-Centered Hole Transporting Material for Efficient Planar Perovskite Solar

Cells, Solar RRL. 2 (2018) 1800048. https://doi.org/https://doi.org/10.1002/solr.201800048.

[14]   E. Sheibani, L. Yang, J. Zhang, Recent Advances in Organic Hole Transporting Materials for

Perovskite Solar Cells, Solar RRL. 4 (2020) 2000461.

https://doi.org/https://doi.org/10.1002/solr.202000461.

[15]   E. Aktas, N. Phung, H. Köbler, D.A. González, M. Méndez, I. Kafedjiska, S.-H. Turren-Cruz, R.

Wenisch, I. Lauermann, A. Abate, E. Palomares, Understanding the perovskite/self-assembled

selective contact interface for ultra-stable and highly efficient p–i–n perovskite solar cells,

Energy & Environmental Science. 14 (2021) 3976–3985.

https://doi.org/10.1039/D0EE03807E.

[16]   A. Al-Ashouri, A. Magomedov, M. Roß, M. Jošt, M. Talaikis, G. Chistiakova, T. Bertram, J.A.

Márquez, E. Köhnen, E. Kasparavičius, S. Levcenco, L. Gil-Escrig, C.J. Hages, R. Schlatmann, B.

Rech, T. Malinauskas, T. Unold, C.A. Kaufmann, L. Korte, G. Niaura, V. Getautis, S. Albrecht,

Conformal monolayer contacts with lossless interfaces for perovskite single junction and

monolithic tandem solar cells, Energy & Environmental Science. 12 (2019) 3356–3369.

https://doi.org/10.1039/C9EE02268F.

[17]   K. Mahmood, S. Sarwar, M.T. Mehran, Current status of electron transport layers in

perovskite solar cells: materials and properties, RSC Advances. 7 (2017) 17044–17062.

https://doi.org/10.1039/C7RA00002B.

[18]   L. Lin, T.W. Jones, T.C.-J. Yang, N.W. Duffy, J. Li, L. Zhao, B. Chi, X. Wang, G.J. Wilson, Inorganic Electron Transport Materials in Perovskite Solar Cells, Advanced Functional Materials. 31 (2021) 2008300. https://doi.org/https://doi.org/10.1002/adfm.202008300.

[19]   J.J. Yoo, S. Wieghold, M.C. Sponseller, M.R. Chua, S.N. Bertram, N.T.P. Hartono, J.S. Tresback, E.C. Hansen, J.-P. Correa-Baena, V. Bulović, T. Buonassisi, S.S. Shin, M.G. Bawendi, An interface stabilized perovskite solar cell with high stabilized efficiency and low voltage loss, Energy & Environmental Science. 12 (2019) 2192–2199. https://doi.org/10.1039/C9EE00751B.

[20]   A. Matas Adams, J.M. Marin-Beloqui, G. Stoica, E. Palomares, The influence of the mesoporous TiO_2 scaffold on the performance of methyl ammonium lead iodide (MAPI) perovskite solar cells: charge injection, charge recombination and solar cell efficiency relationship, Journal of Materials Chemistry A. 3 (2015) 22154–22161. https://doi.org/10.1039/C5TA06041A.

[21]   Z. Zhu, X. Zheng, Y. Bai, T. Zhang, Z. Wang, S. Xiao, S. Yang, Mesoporous SnO_2 single crystals as an effective electron collector for perovskite solar cells, Physical Chemistry Chemical Physics. 17 (2015) 18265–18268. https://doi.org/10.1039/C5CP01534K.

[22]   G. Ren, W. Han, Y. Deng, W. Wu, Z. Li, J. Guo, H. Bao, C. Liu, W. Guo, Strategies of modifying spiro-OMeTAD materials for perovskite solar cells: a review, Journal of Materials Chemistry A. 9 (2021) 4589–4625. https://doi.org/10.1039/D0TA11564A.

[23]   M. Saliba, S. Orlandi, T. Matsui, S. Aghazada, M. Cavazzini, J.-P. Correa-Baena, P. Gao, R. Scopelliti, E. Mosconi, K.-H. Dahmen, F. De Angelis, A. Abate, A. Hagfeldt, G. Pozzi, M. Graetzel, M.K. Nazeeruddin, A molecularly engineered hole-transporting material for efficient perovskite solar cells, Nature Energy. 1 (2016) 15017. https://doi.org/10.1038/nenergy.2015.17.

[24]   F.M. Rombach, S.A. Haque, T.J. Macdonald, Lessons learned from spiro-OMeTAD and PTAA in perovskite solar cells, Energy & Environmental Science. 14 (2021) 5161–5190. https://doi.org/10.1039/D1EE02095A.

[25]   Y. Hua, P. Liu, Y. Li, L. Sun, L. Kloo, Composite Hole-Transport Materials Based on a Metal-Organic Copper Complex and Spiro-OMeTAD for Efficient Perovskite Solar Cells, Solar RRL. 2 (2018) 1700073. https://doi.org/https://doi.org/10.1002/solr.201700073.

[26]   W. Yu, J. Zhang, X. Wang, X. Liu, D. Tu, J. Zhang, X. Guo, C. Li, A Dispiro-Type Fluorene-Indenofluorene-Centered Hole Transporting Material for Efficient Planar Perovskite Solar Cells, Solar RRL. 2 (2018) 1800048. https://doi.org/https://doi.org/10.1002/solr.201800048.

[27]   S. Gangala, R. Misra, Spiro-linked organic small molecules as hole-transport materials for perovskite solar cells, Journal of Materials Chemistry A. 6 (2018) 18750–18765. https://doi.org/10.1039/C8TA08503J.

[28]   J.-Y. Shao, Y.-W. Zhong, Design of small molecular hole-transporting materials for stable and high-performance perovskite solar cells, Chemical Physics Reviews. 2 (2021) 021302. https://doi.org/10.1063/5.0051254.

[29]   X.-D. Zhu, F. Wu, C.-C. Peng, L.-Y. Ding, Y.-J. Yu, Z.-Q. Jiang, L.-N. Zhu, L.-S. Liao, Asymmetrical planar acridine-based hole-transporting materials for highly efficient perovskite solar cells, Chemical Engineering Journal. 413 (2021) 127440. https://doi.org/https://doi.org/10.1016/j.cej.2020.127440.

[30]   L.A. Illicachi, J. Urieta-Mora, J. Calbo, J. Aragó, C. Igci, I. García-Benito, C. Momblona, B. Insuasty, A. Ortiz, C. Roldán-Carmona, A. Molina-Ontoria, E. Ortí, N. Martín, M.K. Nazeeruddin, Azatruxene-Based, Dumbbell-Shaped, Donor–π-Bridge–Donor Hole-Transporting Materials for Perovskite Solar Cells, Chemistry – A European Journal. 26 (2020) 11039–11047. https://doi.org/https://doi.org/10.1002/chem.202002115.

[31]   X. Sun, F. Wu, C. Zhong, L. Zhu, Z. Li, A structure–property study of fluoranthene-cored hole-transporting materials enables 19.3% efficiency in dopant-free perovskite solar cells, Chemical Science. 10 (2019) 6899–6907. https://doi.org/10.1039/C9SC01697J.

[32]   X. Liu, E. Rezaee, H. Shan, J. Xu, Y. Zhang, Y. Feng, J. Dai, Z.-K. Chen, W. Huang, Z.-X. Xu, Dopant-free hole transport materials based on alkyl-substituted indacenodithiophene for planar perovskite solar cells, Journal of Materials Chemistry C. 6 (2018) 4706–4713. https://doi.org/10.1039/C8TC00385H.

[33]   P. Murugan, T. Hu, X. Hu, Y. Chen, Advancements in organic small molecule hole-transporting materials for perovskite solar cells: past and future, Journal of Materials Chemistry A. 10 (2022) 5044–5081. https://doi.org/10.1039/D1TA11039J.

[34]   A.L. Capodilupo, L. de Marco, G.A. Corrente, R. Giannuzzi, E. Fabiano, A. Cardone, G. Gigli, G. Ciccarella, Synthesis and characterization of a new series of dibenzofulvene based organic dyes for DSSCs, Dyes and Pigments. 130 (2016) 79–89. https://doi.org/https://doi.org/10.1016/j.dyepig.2016.02.030.

[35]   A.-L. Capodilupo, R. Giannuzzi, G.A. Corrente, L. de Marco, E. Fabiano, A. Cardone, G. Gigli, G. Ciccarella, Synthesis and photovoltaic performance of dibenzofulvene-based organic sensitizers for DSSC, Tetrahedron. 72 (2016) 5788–5797. https://doi.org/https://doi.org/10.1016/j.tet.2016.08.006.

[36]   G.A. Corrente, E. Fabiano, L. de Marco, G. Accorsi, R. Giannuzzi, A. Cardone, G. Gigli, G. Ciccarella, A.-L. Capodilupo, Effects of donor position on dibenzofulvene-based organic dyes for photovoltaics, Journal of Materials Science: Materials in Electronics. 28 (2017) 8694–8707. https://doi.org/10.1007/s10854-017-6594-2.

[37]   H.-C. Lin, L.-Y. Chen, C.-C. Lu, J.-Y. Lai, Y.-C. Chen, Y.-J. Hung, Ambipolar carrier transport properties of triphenylamine/dibenzofulvene derivative and its application for efficient n-i-p

perovskite solar cells, Organic Electronics. 95 (2021) 106200.

https://doi.org/https://doi.org/10.1016/j.orgel.2021.106200.

[38] E. Zhu, J. Wang, J. Xu, L. Fu, R. Li, C. Yu, S. Ge, X. Lin, R. Chen, H. Wu, H. Wang, G. Che,

Efficient Inverted Perovskite Solar Cells Enabled by Dopant-Free Hole-Transporting Materials

Based on Dibenzofulvene-Bridged Indacenodithiophene Core Attaching Varying Alkyl Chains,

ACS Applied Materials & Interfaces. 13 (2021) 13254–13263.

https://doi.org/10.1021/acsami.0c22993.

[39] M. Leoncini, A.-L. Capodilupo, D. Altamura, C. Giannini, G. Accorsi, E. Fabiano, A. Rizzo, G.

Gigli, S. Gambino, Correlating the chemical structure and charge transport ability of

dibenzofulvene-based hole transporting materials for stable perovskite solar cells, Journal of

Materials Chemistry C. 10 (2022) 5981–5993. https://doi.org/10.1039/D1TC05690E.

[40] Y.-C. Chen, Y.-H. Li, C.-L. Chung, H.-L. Hsu, C.-P. Chen, Triphenylamine dibenzofulvene–

derived dopant-free hole transporting layer induces micrometer-sized perovskite grains for

highly efficient near 20% for p-i-n perovskite solar cells, Progress in Photovoltaics: Research

and Applications. 28 (2020) 49–59. https://doi.org/https://doi.org/10.1002/pip.3205.

[41] A. Beneduci, G.A. Corrente, E. Fabiano, V. Maltese, S. Cospito, G. Ciccarella, G. Chidichimo, G.

Gigli, A.-L. Capodilupo, Orthogonal electronic coupling in multicentre arylamine mixed-

valence compounds based on a dibenzofulvene–thiophene conjugated bridge, Chemical

Communications. 53 (2017) 8960–8963. https://doi.org/10.1039/C7CC03156D.

[42] G.A. Corrente, E. Fabiano, F. Manni, G. Chidichimo, G. Gigli, A. Beneduci, A.-L. Capodilupo,

Colorless to All-Black Full-NIR High-Contrast Switching in Solid Electrochromic Films Prepared

with Organic Mixed Valence Systems Based on Dibenzofulvene Derivatives, Chemistry of

Materials. 30 (2018) 5610–5620. https://doi.org/10.1021/acs.chemmater.8b01665.

[43]	B. Shen, Z. Hu, H. Xu, K. Sun, S. Feng, J. Zhang, Y. Zhu, Investigation of Spiro-OMeTAD Single Crystals toward Optoelectronic Applications, Crystal Growth & Design. 19 (2019) 3272–3278. https://doi.org/10.1021/acs.cgd.9b00124.

[44]	D. Poplavskyy, J. Nelson, Nondispersive hole transport in amorphous films of methoxy-spirofluorene-arylamine organic compound, Journal of Applied Physics. 93 (2002) 341–346. https://doi.org/10.1063/1.1525866.

[45]	S. Li, Y.-L. Cao, W.-H. Li, Z.-S. Bo, A brief review of hole transporting materials commonly used in perovskite solar cells, Rare Metals. 40 (2021) 2712–2729. https://doi.org/10.1007/s12598-020-01691-z.

[46]	M. Jin, H. Li, Q. Lou, Q. Du, Q. Huang, Z. Shen, F. Li, C. Chen, Toward high-efficiency stable 2D/3D perovskite solar cells by incorporating multifunctional CNT:TiO2 additives into 3D perovskite layer, EcoMat. 4 (2022) e12166. https://doi.org/https://doi.org/10.1002/eom2.12166.

[47]	S. Dong, A. Valerio, C. Riccardo, Y. Mingjian, A. Erkki, B. Andrei, C. Yin, H. Sjoerd, R. Alexander, K. Khabiboulakh, L. Yaroslav, Z. Xin, D.P. A, M.O. F, S.E. H, B.O. M, Low trap-state density and long carrier diffusion in organolead trihalide perovskite single crystals, Science (1979). 347 (2015) 519–522. https://doi.org/10.1126/science.aaa2725.

[48]	S.N. Habisreutinger, T. Leijtens, G.E. Eperon, S.D. Stranks, R.J. Nicholas, H.J. Snaith, Carbon Nanotube/Polymer Composites as a Highly Stable Hole Collection Layer in Perovskite Solar Cells, Nano Letters. 14 (2014) 5561–5568. https://doi.org/10.1021/nl501982b.
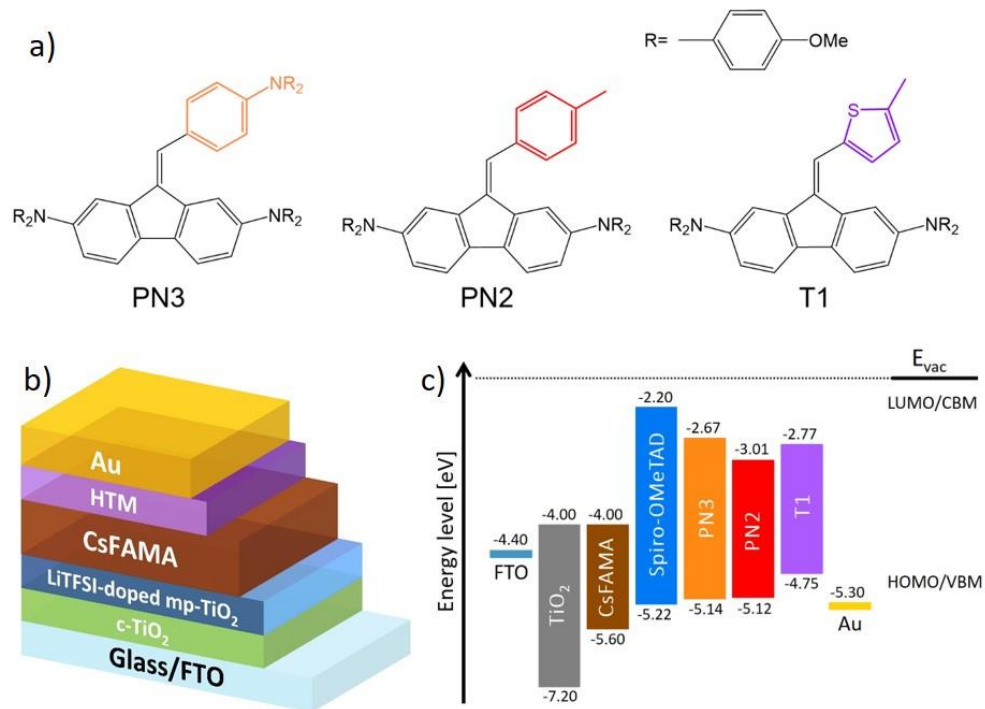
Figure 1. a) Chemical structures of **PN3**, **PN2** and **T1**; b) Scheme of devices structure; c) Energy

levels of three different **DBF**-based HTMs compared with the energy levels of Spiro-OMeTAD.

Table 1. Best-performing parameters of PSCs using Spiro-OMeTAD and different **DBF**-based HTMs. HI indicates the hysteresis index.

HTM	Scan	J_{SC} [mA/cm²]	Integrated J_{SC} [mA/cm²]	V_{OC} [V]	FF [%]	Best PCE [%]	Average[a] PCE [%]	HI
Spiro-OMeTAD	Forward	21.85		0.997	51.24	11.16	11.51 ±1.38	
			20.12					0.37
	Reverse	21.86		1.086	74.73	17.75	16.61 ±0.62	
PN3	Forward	20.85		0.936	48.66	9.50	8.30 ±1.06	
			18.93					0.41
	Reverse	20.83		1.046	73.82	16.08	15.50 ±0.43	
	Forward	21.62		0.875	33.93	6.42	6.07 ±0.78	
PN2			19.79					0.58
	Reverse	21.59		0.952	74.38	15.29	13.99 ±0.79	
	Forward	18.36		0.896	28.28	4.65	4.74 ±0.51	
T1			18.36					0.66
	Reverse	20.33		0.918	72.50	13.53	12.85 ±0.57	

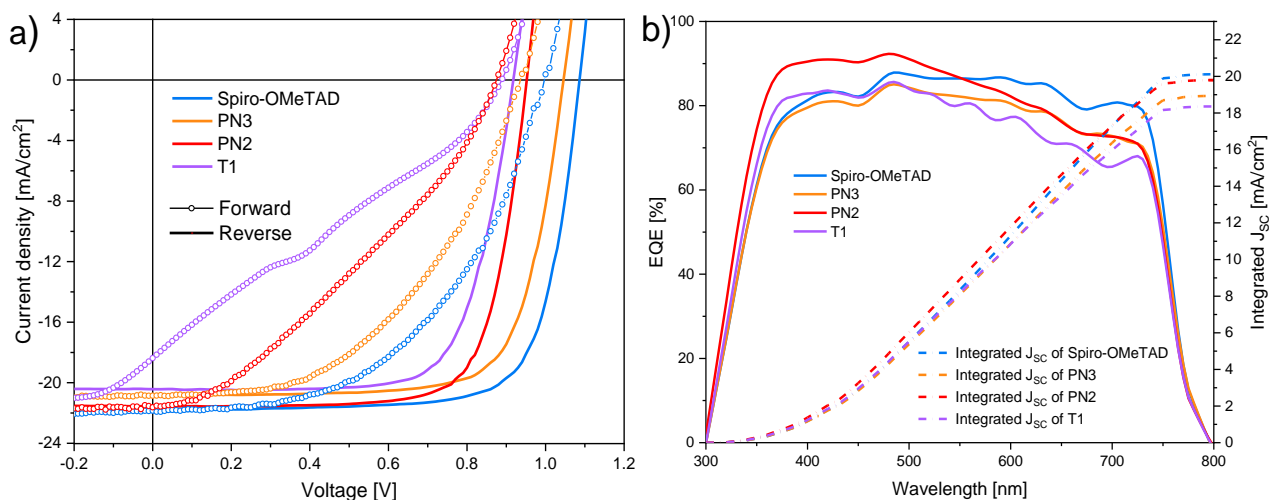[a]Average PCEs were calculated from at least 8 samples.

Figure 2. a) *J-V* characteristics under standard illumination conditions (forward scan in symbols and reverse scan in solid lines); b) EQE spectra (solid lines) and integrated short-circuit current density (dashed lines) of PSCs employing Spiro-OMeTAD and three different **DBF**-based HTMs.
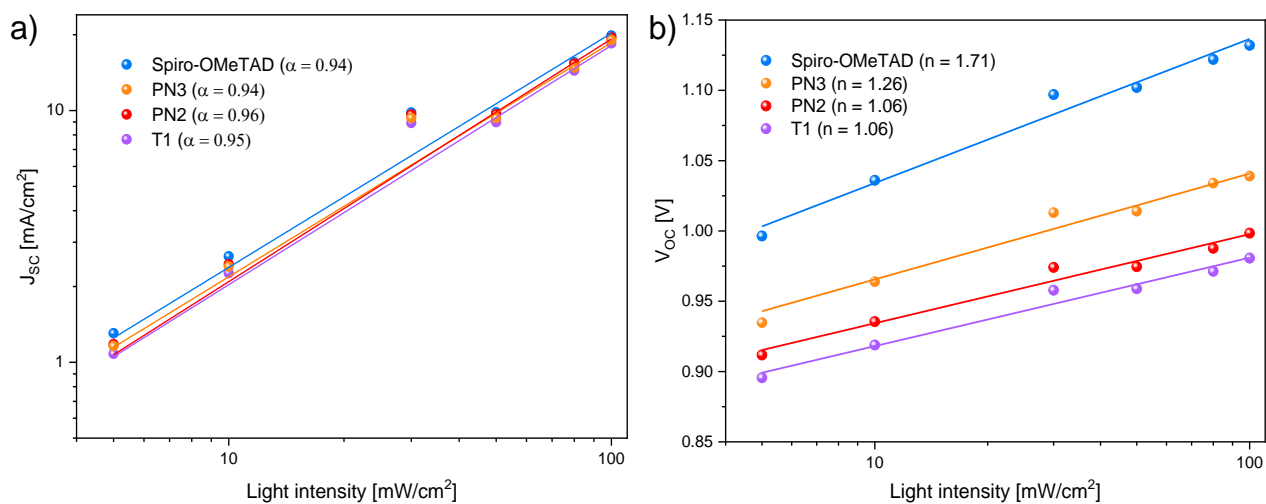

Figure 3. Light intensity dependence of a) J_{SC} and b) V_{OC} of the PSCs with **DBF**-based HTMs and Spiro-OMeTAD. Symbols: experimental data, and solid lines: linear fit.
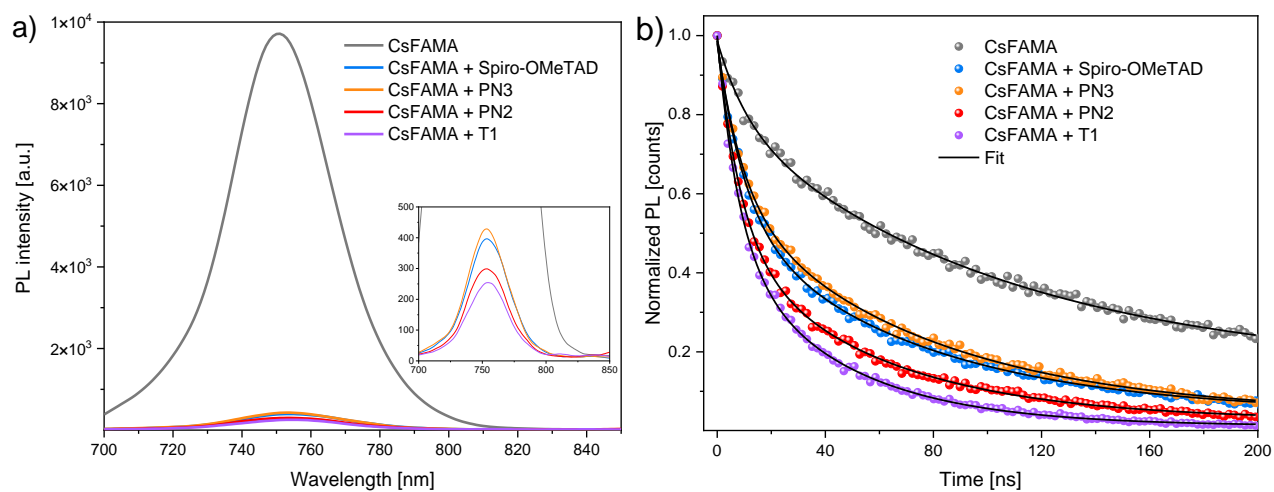
Figure 4. a) Steady-state photoluminescence spectra; b) Normalized time-resolved

photoluminescence spectra of neat CsFAMA, and CsFAMA/HTMs after excitation with a 635nm

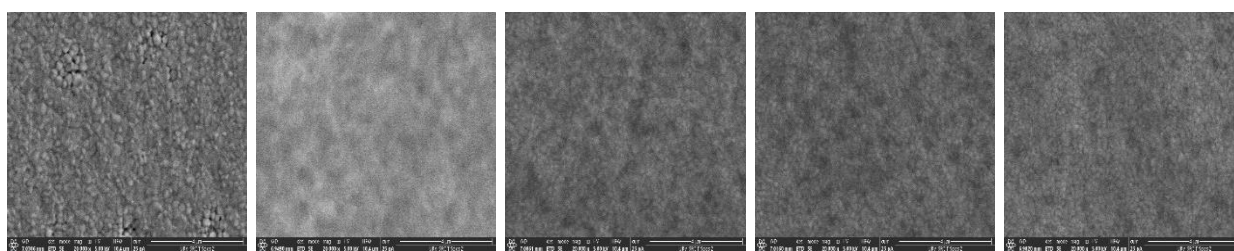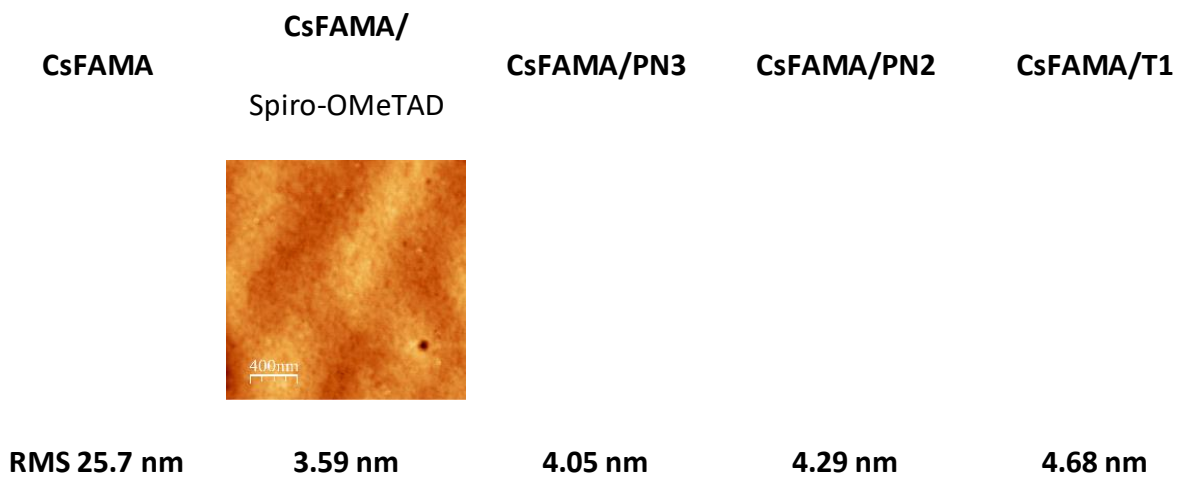laser. Symbols: experimental data, lines: bi-exponential decay fit.

| | CsFAMA/ | | | |
| CsFAMA | Spiro-OMeTAD | CsFAMA/PN3 | CsFAMA/PN2 | CsFAMA/T1 |

| RMS 25.7 nm | 3.59 nm | 4.05 nm | 4.29 nm | 4.68 nm |

Figure 5. AFM height (top) and phase (middle) images of the HTM deposited on top of the FTO/TiO2 dense/TiO$_2$ mesoporous. The film of the perovskite is shown on the left as a reference. The scan size is 1 x 1 µm. FESEM images (bottom) are of the films of HTMs deposited on top of the perovskite.
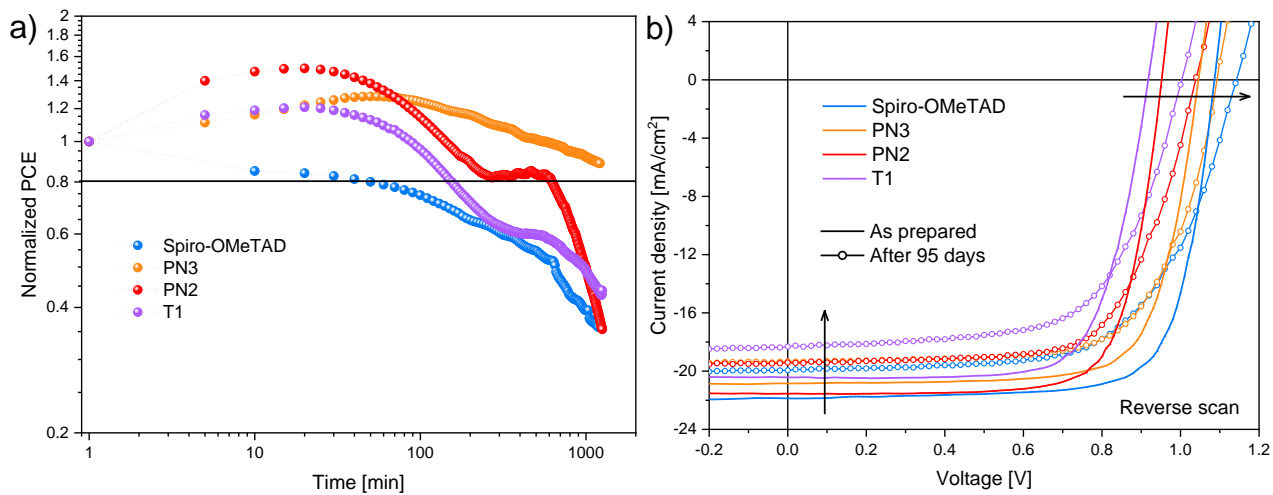
Figure 6. Stability monitoring of PSCs with **DBF**-based HTMs and Spiro-OMeTAD. a) Normalized

PCEs of devices in continuous one sun illumination under ambient conditions (15 ± 2 °C and 60 ±

5% RH) without encapsulation; b) *J-V* curves evolution of devices with **DBF**-based HTMs and Spiro-

OMeTAD stored under dark conditions with constant synthetic airflow of ~10 %RH over 90 days.
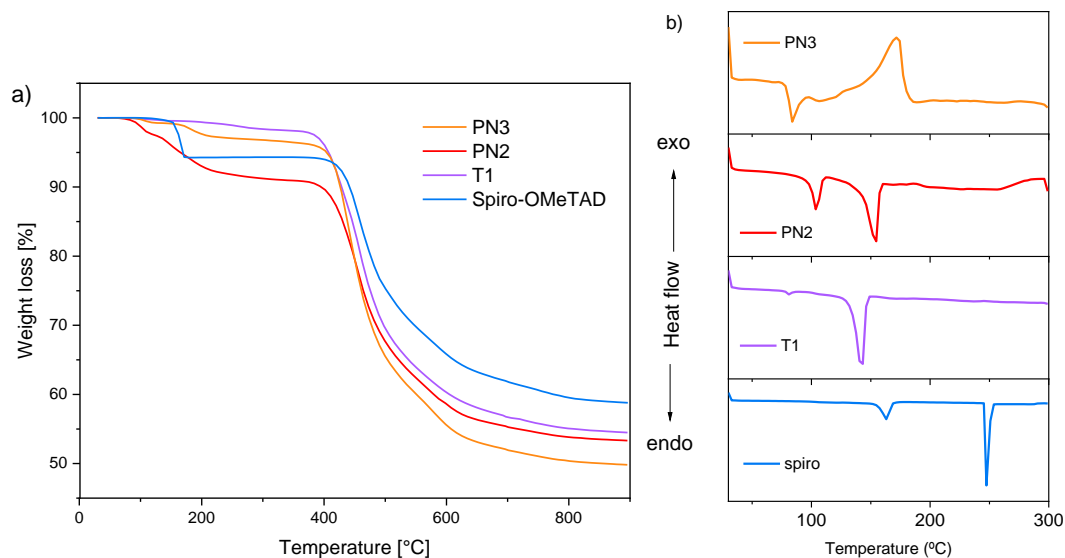
SUPPLEMENTARY INFORMATION

Figure S1. Thermogravimetric (a) and Differential Scanning Calorimetry (b) curves for DBF-based HTMs and Spiro-OMeTAD.

Table S1. Weight loss percentage and associated temperature for each of the HTMs

HTM	Step 1 % Weight loss/ Temperature (°C)	Step 2 % Weight loss/ Temperature (°C)
Spiro-OMeTAD	5.7/ 163	35.5/ 456
T1	1.71/ 115, 257	43.7/ 455
PN2	8.95/ 103, 147	47.4/ 454, 580 sh
PN3	3.01/ 105, 181	46.9/ 439, 585 sh

Table S2. Temperature of the transition and enthalpy associated for each of the HTMs

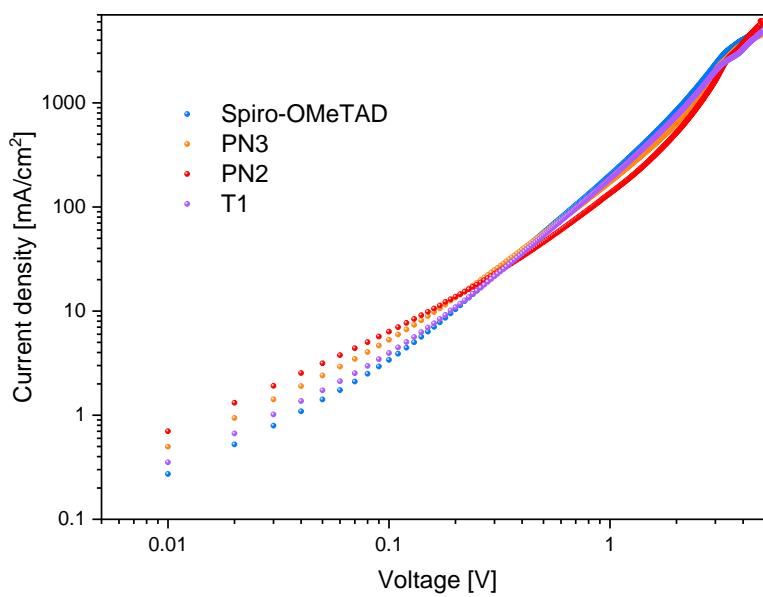| HTM	Temperature of the transition (°C)	Enthalpy (mJ)
Spiro-OMeTAD	163.3	-97.8
	247.7	-256.6
T1	81.1	-2.98
	142.1	-121.8
PN2	98.3	-53.81
	153.85	-133.5
PN3	83.46	-18.8
	171.9	116.5

Figure S2. *J-V* characteristics of hole-only devices fabricated with DBF-based HTMs and Spiro-OMeTAD.

Table S3. Hole-mobility from hole-only devices: ITO/PEDOT/HTM/Au

HTM	Spiro-OMeTAD	PN3	PN2	T1
Hole mobility [10^{-4} cm^2/Vs]	7.41	0.92	0.45	1.1

Table S4. Lifetime results from TRPL decays fitted by a bi-exponential equation.

Film	A_1	τ_1 [ns]	A_2	τ_2 [ns]	$\tau_{Average}$[a] [ns]
CsFAMA	0.19	10.87	0.65	103.41	100.65
CsFAMA/Spiro-OMeTAD	0.45	10.01	0.50	70.22	63.37
CsFAMA/PN3	0.39	9.49	0.55	73.32	67.95
CsFAMA/PN2	0.52	8.76	0.45	56.13	48.89
CsFAMA/T1	0.53	7.88	0.46	42.79	36.68

[a] Average lifetime calculated from the equation: $\tau_{average} = \sum \alpha_i \tau_i$; where $\alpha_i = \frac{A_i \tau_i}{\sum A_i \tau_i}$
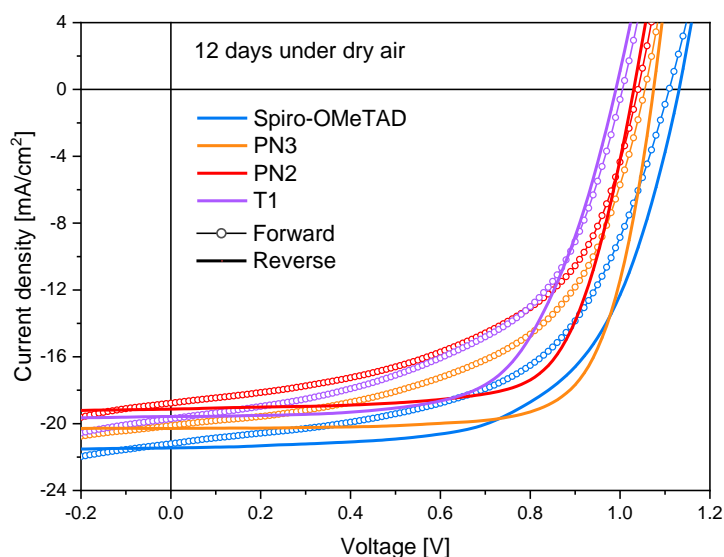
Figure S3. *J-V* characteristics under standard illumination conditions after 12 storing days of devices fabricated with DBF-based HTMs and Spiro-OMeTAD.

Table S5. Performance parameters of PSCs using **Spiro-OMeTAD** and different **DBF**-based HTMs after 12 days storing under dry airflow and dark conditions

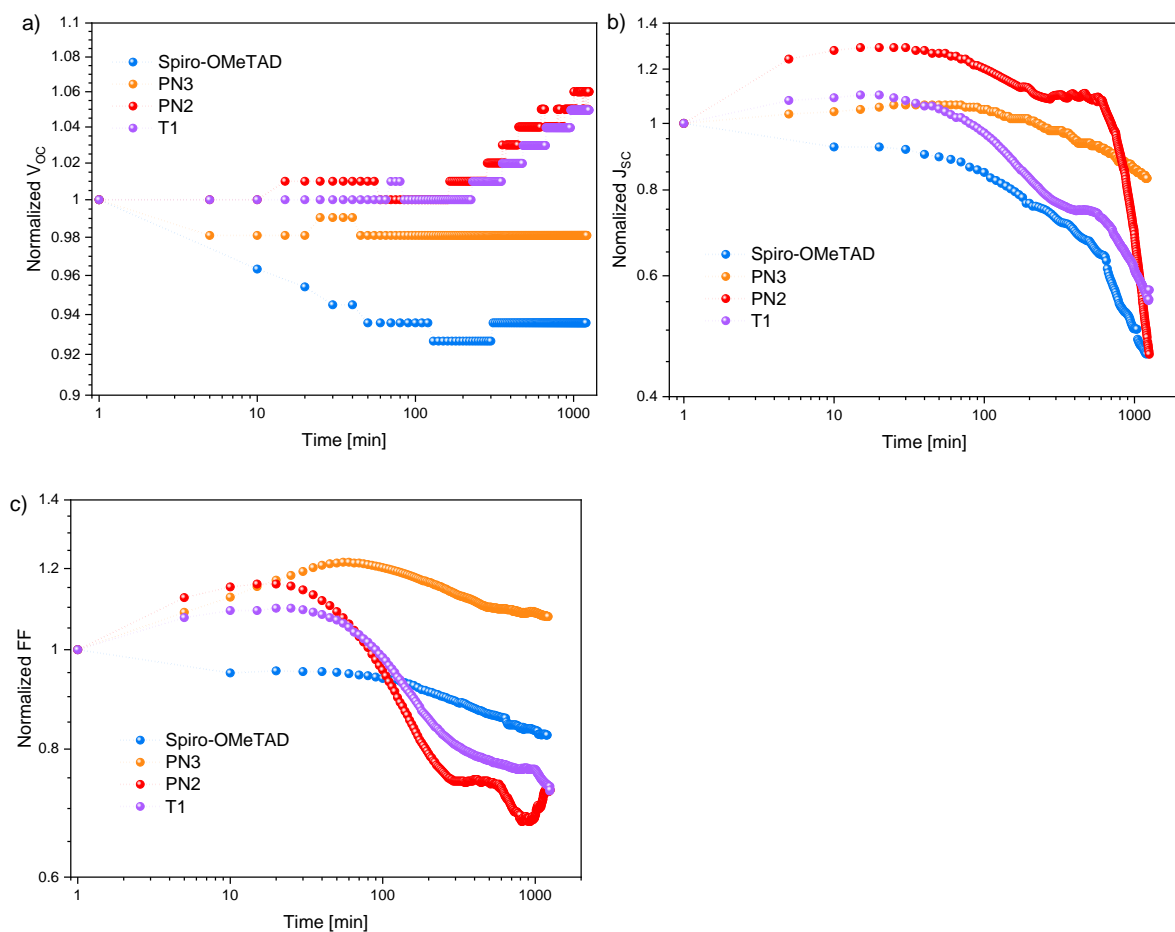| HTM	Scan	J_{SC} [mA/cm^2]	V_{OC} [V]	FF [%]	PCE [%]	HI
Spiro-OMeTAD	Forward	20.01	1.12	0.51	11.27	0.32
	Reverse	20.23	1.15	0.71	16.48	
PN3	Forward	20.14	1.06	0.55	11.76	0.27
	Reverse	20.28	1.08	0.74	16.17	
PN2	Forward	18.80	1.04	0.54	10.50	0.25
	Reverse	19.13	1.03	0.71	14.09	
T1	Forward	19.50	1.00	0.51	9.90	0.22
	Reverse	19.75	0.99	0.65	12.63	

Figure S4. Monitoring of the evolution with time of V_{OC} (a), J_{SC} (b), and FF (c) of devices fabricated with DBF-based HTMs and Spiro-OMeTAD in continuous one sun illumination under ambient conditions.
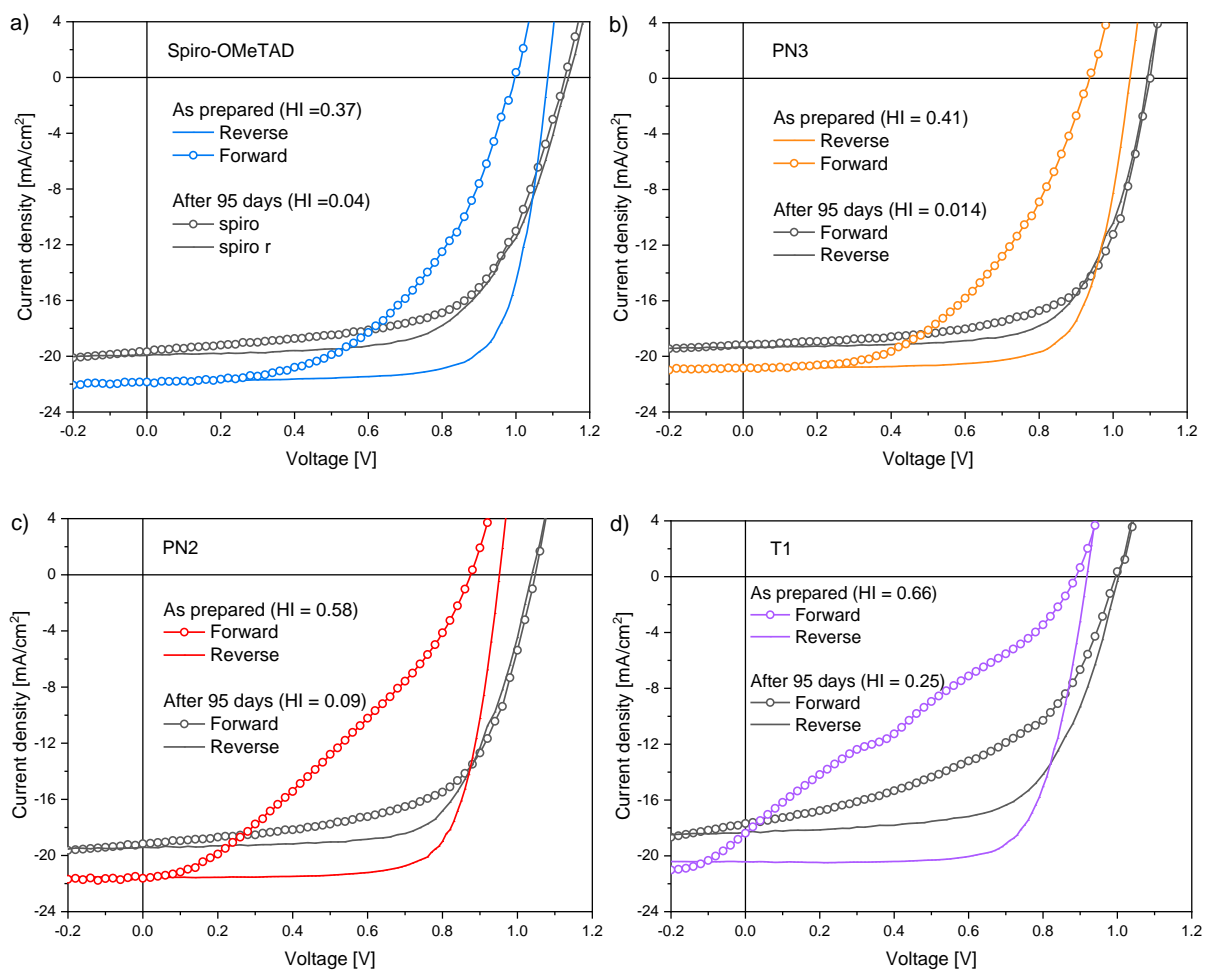
Figure S5. J-V characteristics of PSCs fabricated with Spiro-OMeTAD (a), PN3 (b), PN2 (c), and T1 (d)

HTMs after 95 days stored under dry airflow and dark conditions.

Table S6. Performance parameters of PSCs using **Spiro-OMeTAD** and different **DBF**-based HTMs after 95 days storing under dry airflow and dark conditions

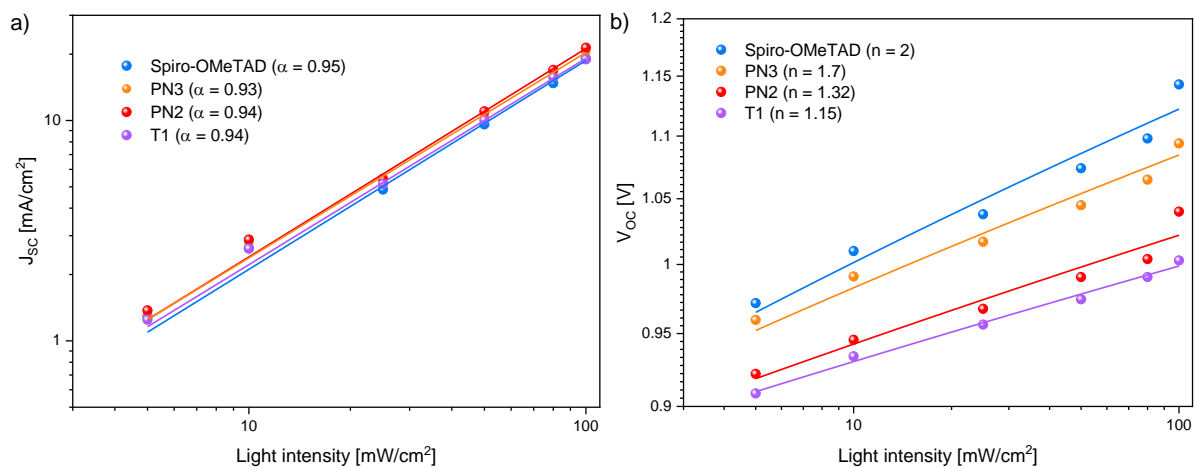| HTM	Time (days)	J_{SC} [mA/cm²]	V_{OC} [V]	FF [%]	PCE [%]	PCE decrement [%]	R_s [$\Omega\cdot cm^2$]
Spiro-OMeTAD	As prep.	21.86	1.086	74.73	17.75		4.34
						19	
	95	19.92	1.142	62.81	14.31		10.21
PN3	As prep.	20.83	1.046	73.82	16.08		5.18
						10	
	95	19.36	1.093	68.41	14.46		6.58
PN2	As prep.	21.59	0.952	74.38	15.29		4.41
						11	
	95	19.44	1.039	67.42	13.59		8.62
T1	As prep.	20.33	0.918	72.50	13.53		5.59
						14	
	95	18.32	1.003	63.43	11.65		9.43

Figure S6. Light intensity dependence of a) J_{SC} and b) V_{OC} of the PSCs with DBF-based HTMs and Spiro-OMeTAD after 95 days storing under dry airflow and dark conditions. Symbols: experimental data, and solid lines: linear fit.